

Native structure of flagellar MS ring is formed by 34 subunits with 23-fold and 11-fold subsymmetries

Akihiro Kawamoto^{1,2,7}, Tomoko Miyata^{1,7}, Fumiaki Makino^{1,3}, Miki Kinoshita¹, Tohru Minamino¹, Katsumi Imada⁴, Takayuki Kato^{1,2} and Keiichi Namba^{1,5,6}

¹ Graduate School of Frontier Biosciences, Osaka University, 1-3 Yamadaoka, Suita, Osaka 565-0871, Japan

² Institute for Protein Research, Osaka University, 3-2 Yamadaoka, Suita, Osaka 565-0871, Japan

³ JEOL Ltd.; 3-2-1 Musashino, Akishima, Tokyo 196-8558 Japan

⁴ Department of Macromolecular Science, Graduate School of Science, Osaka University, 1-1 Machikaneyama-cho, Toyonaka, Osaka 560-0043, Japan

⁵ RIKEN Center for Biosystems Dynamics Research and Spring-8 Center, 1-3 Yamadaoka, Suita, Osaka 565-0871, Japan

⁶ JEOL YOKOGUSHI Research Alliance Laboratories, Osaka University, 1-3 Yamadaoka, Suita, Osaka 565-0871, Japan

⁷ These authors contributed equally: Akihiro Kawamoto, Tomoko Miyata

Correspondence and requests for materials should be addressed to K.N. (email: keiichi@fbs.osaka-u.ac.jp) or T.K. (email: tkato@protein.osaka-u.ac.jp).

29 Abstract

30 **The bacterial flagellar MS ring is a transmembrane complex acting as the core of the**
 31 **flagellar motor. It not only acts as the template for rod and C ring assembly but also**
 32 **houses the type III protein export gate for assembly of the rod, hook and filament. The**
 33 **cytoplasmic C ring, involved in torque generation and rotation switch, is directly**
 34 **attached to the MS ring, and a symmetry mismatch between 26-fold MS ring and**
 35 **34-fold C ring had been a long puzzle as to whether this would play some role in motor**
 36 **function. Although this puzzle seemed to have been resolved by the recent**
 37 **high-resolution structure of the MS ring with 33-fold symmetry with a variation from**
 38 **32-fold to 35-fold because the C ring also shows a similar symmetry variation, it still**
 39 **remained ambiguous whether their symmetries are matched in the native motor**
 40 **structure. Here we show that the native MS ring structure formed by full-length FliF is**
 41 **34-fold with no symmetry variation whereas the C ring has a small symmetry variation,**
 42 **indicating a flexibility in C ring assembly to generate small symmetry mismatches. We**
 43 **also show two conformations of FliF in part of its periplasmic region to form the**
 44 **34-subunit ring with 23-fold and 11-fold subsymmetries in the inner and middle M ring,**
 45 **respectively, to accommodate the export gate at the center of the M ring.**

46
 47
 48 Bacteria actively swim in liquid environments by rotating long, helical filamentous organelle
 49 called the flagellum. The bacterial flagellum is supramolecular motility machinery consisting
 50 of the basal body that acts as a bi-directional rotary motor, the filament that functions as a
 51 helical propeller, and the hook as a universal joint connecting the basal body and the filament
 52 to transmit motor torque to the filament¹⁻³. The basal body consists of the MS ring, C ring, LP
 53 ring and the rod (Fig. 1a). The MS ring is a transmembrane protein complex made of FliF and
 54 is the base for flagellar structure, assembly and function. The MS ring is not only the
 55 mounting platform for the C ring, which is the cytoplasmic part of the basal body formed by
 56 the switch proteins FliG, FliM and FliN and acts as a bi-directional rotor of the flagellar
 57 motor as well as the switch regulator of the rotation direction, but is also a housing for the
 58 type III protein export apparatus that exports flagellar axial proteins for their assembly at the
 59 distal growing end of the flagellum²⁻⁴. The rod is a drive shaft of the motor, transmitting
 60 motor torque to the hook and filament and is a helical assembly of four different rod proteins,
 61 FlgB, FlgC, FlgF and FlgG. The LP ring is a bushing tightly embedded in the peptidoglycan
 62 layer as well as the outer membrane and surrounds the distal, thicker tubular part of the rod

63 formed mainly by FlgG^{5,6} to stabilize the high speed rotation of the motor¹⁻³. Motor torque
64 is generated by cyclic interactions and dissociation of FliG at the top end of the C ring with
65 the cytoplasmic domain of the transmembrane stator complex formed by MotA and MotB,
66 which also acts as a proton channel to couple proton influx across the membrane with torque
67 generation⁷, where multiple number of stator units surround the rotor to become active
68 depending on the external load⁸.

69 For a long time until recently, the MS ring had been believed to have 26-fold rotational
70 symmetry whereas the C ring has 34-fold symmetry with some minor variations based on
71 biochemical and structural studies⁹⁻¹³. This symmetry mismatch between the two rotor
72 complexes had been a focus of debates on its possible role in the C ring assembly, torque
73 generation and stepping rotation and the basis for the mechanistic understanding of torque
74 generation mechanism^{11,14,15}. This puzzle was sort of resolved by the recent high-resolution
75 structure of the MS ring with 33-fold symmetry with a variation from 32 to 35 (ref. ¹⁶)
76 because the C ring also shows a similar symmetry variation peaked around 34- or 35-fold^{12,17}.
77 However, it still remained ambiguous whether their symmetries are actually matched in the
78 native motor structure, because the distributions of the symmetry variations are clearly
79 different between the two rings, with a peak around 34- or 35-fold for the C ring^{12,17} and
80 33-fold for the MS ring¹⁶. Also, the MS ring structures were analyzed for those formed by
81 overexpressed FliF with some C-terminal truncations¹⁶, which may have produced the
82 observed symmetry variation.

83 There is also another interesting symmetry mismatch between the MS ring and the rod,
84 which assembles directly on the MS ring while having a helical tubular structure with 11
85 protofilaments, with a helical symmetry of about 5.5 subunits per one turn of helix. The core
86 structure of the type III protein export gate composed of FliP, FliQ and FliR¹⁸ is likely to be
87 located inside the MS ring with a helical nature in their assembly to be directly connected
88 with the proximal part of the rod formed by FlgB, FlgC and FlgF via an adapter protein FliE¹⁹.
89 However, it remains unknown how the symmetry mismatch between the protein export
90 gate-rod and the MS ring is resolved to make flagellar assembly possible by the MS ring as
91 the assembly template.

92 Here we report electron cryomicroscopy (cryoEM) structural analyses of the flagellar
93 basal body and the MS ring formed by full-length FliF from *Salmonella enterica* serovar
94 Typhimurium (hereafter referred to *Salmonella*) and that the symmetry of the native MS ring
95 is 34-fold with no variation. Our own symmetry analysis of the C ring of the basal body
96 showed a variation with a peak at 34-fold in agreement with the previous observation¹²,

indicating that there are still small symmetry mismatches between the two rings possibly generated by some flexibility in the initiation of C ring assembly by FliG around the MS ring. The MS ring structure also showed 23-fold and 11-fold symmetries in the inner and middle parts of the M ring, respectively, possibly to accommodate the type III protein export gate to assemble at the center of the MS ring. The structure of the S ring and cylindrical collar in the upper part of the MS ring is now resolved at high resolution, and mutational analyses show that conserved residues of FliF are responsible not only for MS ring formation by stabilizing intersubunit interactions but also for the assembly of the type III protein export apparatus and the rod within the MS ring. Thus, it is now clear that the MS ring and C ring are tightly bound to each other to act as a rotor unit of the flagellar motor to generate and transmit torque to the rod, hook and filament for bacterial motility.

CryoEM structural analysis of the basal body

We isolated the flagellar basal body from a *Salmonella* mutant strain HK1003 [*flgEA*(9-20) Δ *clpP*::Cm deletion mutant], in which the number of the basal body was increased by the deletion of the ClpP protease²⁰, and analyzed the structure by cryoEM image analysis. Most of the isolated basal bodies are missing the LP ring because the LP ring easily dissociates from the rod in the absence of the hook (Fig. 1b, Extended Data Fig. 1a). This structure is called a rivet because of its shape, and this partial basal body structure is advantageous for visualizing the symmetry of the MS ring in the end-on view because the LP ring normally above the MS ring disturbs the visualization of the MS ring image. The two-dimensional (2D) class average images of its end-on views thus allowed the determination of the MS ring symmetry (Fig. 1c, Extended Data Fig. 1b). Of the 34,896 particle images of the basal body that were picked up from the 1,578 cryoEM micrographs, 23,104 particle images were near end-on views, separated into four classes with slight differences in the orientation, where each of the four class images clearly showed the 34-fold rotational symmetry (Fig. 1c). So the MS ring structure in the native flagellar basal body is composed of 34 FliF subunits.

We also analyzed the symmetry of the C ring of the native flagellar basal body. Although the symmetry of the C ring in the basal body has already been studied by cryoEM image analysis, the previous study used an indirect method in which side view images of the C ring were subjected to multireference alignment against projections of three-dimensional (3D) models with symmetries from 32- to 36-fold to sort the particle images into different rotational symmetries¹², and this may have produced some errors by misalignment and possible deformation of the C ring from a perfect cylinder. We therefore used only end-on

views of the C ring that show blobs of subunits and analyzed the rotational symmetry (Extended Data Fig. 1c). Since the flagellar motor can switch the rotation between the counter-clockwise (CCW) and clockwise (CW) direction, we looked at both CCW and CW locked C ring structures. As shown in Fig. 1d, the C ring symmetry has a certain range of variation from 32- to 35-fold for CCW and 33- to 36-fold for CW, but about two thirds are 34-fold symmetry with rather minor populations of non 34-fold symmetries (CCW: 32-fold, 2%; 33-fold, 20%; 34-fold, 66%; 35-fold, 13%, 36-fold, 0%; CW: 32-fold, 0%; 33-fold, 13%; 34-fold, 68%; 35-fold, 20%; 36-fold, 1%). This is in marked contrast to much higher populations of non 34-fold symmetries (32-fold, 2%; 33-fold, 17%; 34-fold, 42%; 35-fold, 30%; 36-fold, 7%) estimated in the previous study¹². Thus, although the symmetry mismatch between the MS ring and C ring is present, the probabilities of C ring assembly around the MS ring with extra or less FliG subunits to the FliF subunits is small, and the number of extra or less FliG subunits is mostly up to one, indicating that the flexibility in the template driven C ring assembly by FliG around the 34 FliF-subunit MS ring that causes a symmetry mismatch between these two rings is not so high.

CryoEM structural analysis of the MS ring formed by overexpressed FliF

We overexpressed full-length *Salmonella* FliF in *E. coli* and isolated the MS ring from the membrane fraction by sucrose gradient purification (Extended Data Fig. 2a,b). Although the ring-shaped particles were clearly observed in negative stained EM images (Extended Data Fig. 2c), it was difficult to determinate the structure of the MS ring by cryoEM image analysis because most of the particles were attached to the edge of carbon holes. To alleviate such awkward characteristics of the MS ring, we optimized the purification procedure using LMNG as a detergent, which drastically improved the particle dispersion and density in the holes and allowed high quality image data collection in sufficient particle numbers. A total of 339,861 particles were extracted from 1,589 micrographs and were analyzed. Representative 2D class averages showed homogeneous ring particles with clear 34-fold symmetry (Fig. 2a, Extended Data Fig. 3 and 4). We did not observe any other symmetries in the 2D class averages, indicating that the MS ring formed by full length FliF consists of 34 subunits and shows no variation in the ring stoichiometry, just as we observed for the MS ring in the native basal body structure as described above.

We then carried out 3D image reconstruction of the MS ring, but the resolution did not extend beyond 10 Å without rotational symmetry. We therefore performed iterative 3D refinement with 34-fold rotational symmetry. This process dramatically improved the

resolution of the 3D map to 3.7 Å resolution (Extended Data Fig. 3) and enabled us to construct the atomic model of the S ring and collar (Fig. 2b,c). Unfortunately, however, a large part of the M ring was somehow disordered in this particular construct.

The S-ring and collar is formed by residues 228–438 of *Salmonella* FlhF (Fig. 2d), which correspond to the latter half of the periplasmic region. The monomeric structure consists of two structural regions: a globular domain with $\alpha\beta\alpha\beta$ motif that is known as a ring building motif (RBM) (residues 228–270 and 382–438 designated as RBM3 in Fig. 2b); and a long, extended up-and-down β structure (residues 271–381) consisting of a set of antiparallel chains and a set of antiparallel β strands, β 3 and β 4, forming a β hairpin with invisible 51 residues possibly forming a flexible loop (Fig. 2b). The chain connecting β 3 and β 4 at the top of the collar (residues 305–354) was not modeled due to the poor density (Fig. 2b–d). The S ring is made up of 34 RBM3 domains horizontally packed with their major axis oriented in the radial direction to form a ring with a diameter of 24 nm. The long β hairpins in the upper part of the collar are vertically lined up to form a 68-stranded cylindrical β -barrel structure. The two extended antiparallel chains connecting the RBM3 domain and the vertical β hairpin are inclined about 30 degrees from the ring axis. The model was nearly identical to the corresponding part of the recent MS ring structure with 34-fold symmetry¹⁶.

The overall structure of the S-ring and collar resembles the SpoIIIAG structure²¹ despite the low sequence identity (<15%) (Extended Data Fig. 5a,b). The unique large β -barrel structure composed of vertically arranged β -strands is present in the SpoIIIAG ring. The ring arrangement of the RBM3 domains is also similar to that of the SpoIIIAG, although the RBM domain of the SpoIIIAG ring is tilted about 14 degrees compared with the nearly horizontal orientation of that of the S ring (Extended Data Fig. 5a,b). The ring formation through the RBM domain is commonly found in the T3SS injectisome, and the domain arrangement of the S ring is similar to those in the T3SS ring except for the D2 domain of PrgH^{22–26}.

The chain folding arrangement of FlhF in the collar is also similar to those seen in the secretin rings of the type III secretion system (T3SS) of bacterial pathogens²⁷. Unlike them, however, only a small number of hydrogen bonds are formed between these two chains in the flagellar MS ring because the two antiparallel chains are twisted and apart from each other toward the bottom of the cylindrical β -barrel structure, even though the phi-psi angles of each residue in these extend chain are mainly those of the β type conformation. Residues 283–293 connecting to β 3 of the vertical β hairpin is looping out to form a structure that looks like a saucer to the cup upon assembly into the ring. The two antiparallel chains are swapped right and left before connecting to the vertical β hairpin in the upper part of the collar (Extended

Data Fig. 5c).

Mutation analysis of FliF for the MS ring formation

We examined whether the atomic model of the S ring represents the structure of the physiologically functional MS ring of the flagellar basal body by mutations of FliF followed by assays of cell motility, flagellar protein export and assembly of the basal body and MS ring. The subunit interface of the RBM3 domains in the S ring is mainly mediated by the hydrophobic interactions. Ile-252, Leu-253, and Val-266 are relatively well conserved between FliF and SpoIIIAG²¹ (Fig. 3a). Ile-107 and Val-120 of SpoIIIAG corresponds to Ile-252 and Val-266 of FliF, respectively, and the replacement of each residue by Arg inhibits SpoIIIAG ring formation. We therefore replaced Ile-252, Leu-253 and Val-266 by Ala or Arg and analyzed the effects of these mutations on cell motility in soft agar to test whether these three residues are involved in MS ring formation (Fig. 3b). These substitutions did not significantly affect the steady cellular level of FliF as judged by immunoblotting with polyclonal anti-FliF antibody (Fig. 3c). Wild-type FliF fully restored motility of a Δ *fliF* mutant. The V266A mutant variant complemented the Δ *fliF* mutant to the wild-type level, and the L253A mutant variant restored the motility to a considerable degree, but the I252A mutant variant did so only poorly. The I252R, L253R and V266R mutant variants did not complement the Δ *fliF* mutant at all (Fig. 3b). In agreement with this, the I252A and L253A mutants formed a few flagellar filaments but the I252R, L253R and V266R mutants did not at all (Fig. 3d).

The MS ring is also a housing for the flagellar type III protein export apparatus^{28,29}. Therefore, we tested whether the poor flagellar formation by the *fliF*(I252A) and *fliF*(L253A) mutant strains compared with the wild-type and *fliF*(V266A) mutant strains is a consequence of their reduced protein export activity. We examined the secretion levels of the hook-capping protein FlgD, the hook protein FlgE and the filament protein FliC as representative export substrates and found that the reduction in their secretion levels was well correlated with the reduction in the levels of flagellar formation (Fig. 3d,e). These two mutants produced hook-basal bodies (Fig. 3d), indicating that these two mutations do not affect MS ring formation so significantly. Therefore, these results suggest that the I252A and L253A mutations affect the assembly of the type III protein export apparatus into the MS ring. The I252R, L253R and V266R mutations abolished flagellar protein export (Fig. 3e), explaining the complete loss of motility of these mutant strains (Fig. 3b).

The cytoplasmic face of the MS ring is the template for assembly of the C ring by the

switch proteins FliG, FliM and FliN²⁻⁴. Because the C ring is also a housing of the cytoplasmic part of the type III protein export apparatus and the loss of C ring considerably reduces the flagellar protein export activity and thereby impairs the cell motility²⁸, we tested whether the FliF mutations we examined above also affect C ring formation to cause the reduction in cell motility. If the C ring is formed normally on the cytoplasmic face of the MS ring, FliG, FliM and FliN should be detected in the membrane fraction of the cells because the MS ring is a transmembrane complex. Only a very small amount of FliN was found in the membrane fraction of the $\Delta fliF$ mutant as expected, but large amounts of FliN were detected in the membrane fractions of all the *fliF* mutant cells just as observed for wild-type cells (Fig 3c). This suggests that these FliF mutations do not affect C ring formation at all and that mutations of Ile-252, Leu-253 and Val-266 have direct effects on the assembly of the type III protein export gate within the MS ring.

To examine the effect of these FliF mutations on the stability of the MS ring, we purified the MS rings from *E. coli* cells overexpressing these mutant variants of FliF and observed them by negative staining EM. All the FliF mutations significantly affected the stability, and most of the ring-shaped particles of the size of the MS ring were not completely closed (Fig. 3f). Ile-252 is located at the interface between FliF subunits whereas Leu-253 and Val-266 are not, suggesting that Ile-252 is responsible for intermolecular interactions between FliF subunits whereas Leu-253 and Val-266 are involved in proper folding of each FliF subunit to form the S ring. To further confirm this, we carried out *in vitro* disulfide cross-linking experiments.

Since His-263 and Ala-388 are in close proximity to Ile-252 in the atomic model of the S ring (Fig. 3a), we replaced Ile-252, His-263 and Ala-388 by Cys and analyzed cell motility in soft agar plates. Cys mutation of each residue did not drastically affect cell motility. The H263C variant complemented the $\Delta fliF$ mutant to the wild-type level, and the I252C and A388C variants restored the motility to a considerable degree although not to the wild-type level (Fig. 3g). However, neither I252C/H263C nor I252C/A388C double mutation variant complemented the $\Delta fliF$ mutant to restore cell motility, suggesting that crosslinked FliF subunits in the MS ring may have impaired its function, such as insertion of the type III protein export gate into the MS ring. Intersubunit disulfide crosslinking of FliF by the double Cys mutations was confirmed by higher-order oligomeric species observed in the membrane fraction isolated from the *fliF*(I252C/H263C) mutant upon inducing disulfide crosslinking by adding iodine (Fig. 3i, red dots), confirming that the atomic model of the S ring we built here is a physiological one. Such oligomers were observed neither for the wild-type, I252C nor

H263C mutant (Fig. 3i). The appearance of an extra band of FliF monomer with a slightly faster mobility in the SDS-PAGE gel (Fig. 3i, blue dot) can be due to intramolecular disulfide crosslink, suggesting a significantly different conformation of FliF monomer before its assembly into the MS ring. It is also possible that the conformational change of FliF monomer by intramolecular disulfide crosslink disturbs the proper assembly of the MS ring. The replacement of Cys-263 by Tyr in this double Cys FliF mutant considerably restored the motility (Fig. 3h), suggesting a requirement of flexibility in the MS ring structure for its proper function.

Internal structure of the MS ring with 23-fold and 11-fold subsymmetries

The 3D reconstruction of the basal body at about 6.8 Å resolution (Fig. 4a-c, Extended Data Fig. 6) from cryoEM image data shown in Fig. 1b revealed interesting features in the inner core of the M ring in addition to the 34-fold rotational symmetry of the S ring (Fig. 1c). The inner part of the M ring is a flat ring with clear 23-fold symmetry, and its central hole accommodates a helical assembly of many rod-shaped densities possibly representing α -helices, which looks very similar to the structure of the export gate complex formed by FliP, FliQ and FliR¹⁹. As we stated earlier, cryoEM 3D reconstruction of the MS ring structure from an FliF overexpression construct had a large part of the M ring density disordered and therefore not showing its internal feature in detail (Extended Data Fig. 3), but the MS ring formed by FliF overexpressed from another construct produced the entire MS ring density that can be identified in the basal body (Fig. 4c,e, Extended Data Fig. 7). We identified an 11-fold symmetry density features just outside the inner M ring with 23-fold symmetry. Even 2D class average images showed the 11-fold symmetry just outside the collar (Fig. 4d, Extended Data Fig. 7). We therefore enforced 11-fold symmetry on the entire MS ring structure to see which parts of the MS ring have 11-fold symmetry (Fig. 4c). The outer part of the M ring was featureless but the middle part just outside the inner M ring with 23-fold symmetry showed a strong 11-fold symmetry feature as a hinge connecting to the outer M ring. These structural features indicate that the MS ring is formed by 34 FliF subunits with two distinct conformations. All the 34 subunits contribute their RBM3 in the latter half of the periplasmic region of FliF to the S ring and collar, but 23 copies form the inner M ring and 11 copies form the hinge with their RBM1 and RBM2 in the former half of the periplasmic region (Fig. 2 and 4c).

CryoEM structural analysis of the export gate complex formed by FliP, FliQ and FliR overexpressed in *E. coli* has revealed a helical nature of multi-subunit assembly of the

FliP₅FliQ₄FliR (10 subunits) and FliP₅FliQ₄FliR₁FlhB₁ (11 subunits) complexes^{19,30}, and the helical parameter is similar to those of the flagellar axial structures, such as the rod, hook and filament, with about 5.5 subunits per turn of the 1-start helix, which can also be regarded as a tubular structure with 11 protofilaments. However, the 11-fold symmetry feature of the internal part of the M ring is not the one directly associated with the export gate at the center of the M ring. It is the 23-fold symmetry internal core ring of the M ring that forms a hole of the right size to accommodate the export gate at the center of the M ring over a symmetry mismatch.

Discussion

The long-term puzzle on the role of symmetry mismatch between the MS ring with 26-fold rotational symmetry and the C ring with 34-fold symmetry⁹⁻¹³ had produced much debate on its role in the C ring assembly, torque generation and stepping rotation^{11,14,15}. This puzzle was sort of resolved by the recent high-resolution structure of the MS ring with 33-fold symmetry with a variation from 32- to 35-fold¹⁶ because the C ring also shows a similar symmetry variation around 34- or 35-fold^{12,17}. However, it was still not clear whether the symmetries of these two rings are actually matched in the native motor structure, because the distributions of the symmetry variations are clearly different between the two rings, with a peak around 34- or 35-fold for the C ring^{12,17} and around 33-fold for the MS ring¹⁶.

By cryoEM structural analyses of the flagellar basal body isolated from *Salmonella* cells and the MS ring formed by overexpressed full-length FliF of *Salmonella*, we determined the rotational symmetry of the native MS ring structure to be 34-fold with no variation (Fig. 1). The recent high-resolution structures of the MS ring with 33-fold symmetry with some variation would therefore be an artifact, possibly produced by the C-terminal truncations of FliF¹⁶. We also carried out the symmetry analysis of the basal body C ring in a more direct manner than the previous study¹² by looking at enface views of the ring revealing subunit blobs (Extended Data Fig. 1c) and showed a symmetry variation to have a peak at 34-fold with much less populations of non 34-fold symmetry rings. So, the symmetries of the two rings are matched in the majority of the flagellar basal body albeit there are still minor populations having symmetry mismatches of one more or one less subunit in the C ring. The C ring assembly is thought to be initiated by co-folding of the C-terminal chain of FliF extending out on the circumference of the MS ring in the cytoplasm and the N-terminal domain of the FliG^{31,32}. Also, mutation studies of *Salmonella* flagella have identified two types of FliF-FliG fusion proteins that are functional in motility³³. These results predicted a

rather strict 1:1 stoichiometry of FliF and FliG in the C ring assembly around the MS ring. However, our present structural analysis clearly shows symmetry mismatches between the two rings albeit rather small, suggesting a certain level of flexibility in FliG ring assembly around the MS ring to initiate the entire C ring assembly together with the other switch proteins FliM and FliN.

The structure of the S ring and cylindrical collar in the upper part of the MS ring is now resolved at high resolution (Fig. 2), and mutation analyses based on the atomic model show that conserved hydrophobic residues of FliF located at the intersubunit interface are responsible not only for MS ring formation by stabilizing intersubunit interactions but also for the assembly of the type III protein export apparatus and the rod within the MS ring (Fig. 3). Interestingly, The structures of the basal body and MS ring also showed 23-fold and 11-fold symmetries in the inner part of the M ring and a density feature at the center that looks exactly like the protein export gate complex formed by FliP, FliQ and FliR¹⁹ (Fig. 4). Contributing only 23 copies of RBM1-2 of total 34 to the formation of the inner core M ring would possibly be to form the central hole of an appropriate size for the protein export gate to efficiently assemble at the center of the MS ring. Thus, it is now clear that FliF is folded into two distinct conformations to build the MS ring structure with different symmetries in different parts for its multiple functions. This was also suggested by the recent high-resolution structures albeit their detailed features were unfortunately non-physiological ones possibly due to the C-terminal truncations of FliF¹⁶. The folding and assembly of 34 FliF subunits forming the multi-symmetry structure of the native MS ring will be described elsewhere. It is at least confirmed now that the MS ring and C ring are tightly bound to each other to act as a rotor unit of the flagellar motor to generate and transmit torque to the rod, hook and filament for bacterial motility.

Methods

Bacterial strains, plasmids and media

Bacterial strains and plasmids used in this study are listed in Table 1. L-broth and soft tryptone agar plates were prepared as described previously^{28,34}. Ampicillin was added at a final concentration of 100 µg/ml.

Purification of the basal body

Salmonella HK1003 [*flgEA*(9-20) Δ *clpP*::*Cm*] (CCW motor) and TM022 [*flgEA*(9-20) Δ *clpP*::*Cm* *fliG* Δ PAA³⁵] (CW motor) mutant cells, in which the number of the basal body was increased by the deletion of the ClpP protease²⁰, were grown in 5 l of L-broth [1% (w/v) tryptone, 0.5% (w/v) yeast extract, 1% (w/v) NaCl] at 37°C until the cell had reached a late-logarithmic stage. The cells were harvested by centrifugation at 4,600 \times g for 10 min. The pellets were suspended in 240 ml of 50 mM Tris-HCl buffer at pH 8.0 containing 0.5 M sucrose in an ice bath. EDTA and lysozyme were added to final concentrations of 10 mM and 0.1 mg·ml⁻¹, respectively, and the mixture was stirred for 30 min to convert cells to spheroplasts. Triton X-100 and MgSO₄ was added to the mixture to final concentrations of 1% and 10 mM, respectively. After stirring in the ice bath for 1 h, the mixture was centrifuged at 15,000 \times g for 20 min to remove insoluble debris. An aliquot of 5 M NaOH was added to the supernatant to adjust pH to 10.5. The solution was centrifuged at 60,000 \times g for 60 min, and the pellet was suspended in a buffer containing 10 mM Tris-HCl pH8.0, 5 mM EDTA and 1% Triton X-100. After repeating the above procedure twice, the basal body was purified by sucrose density gradient centrifugation at 68,000 \times g for 14 h. Fractions with 20-50% sucrose were collected and centrifuged at 60,000 \times g for 60 min. The pellet was suspended in Buffer S (25 mM Tris-HCl pH 8.0, 1 mM EDTA, 50 mM NaCl) containing 0.05% Triton X-100 and 0.05% LMNG or Buffer I (50 mM Tris-HCl pH 8.0, 50 mM NaCl, 25 mM imidazole, 0.05% Triton X-100 and 0.05% LMNG).

Overexpression of FlhF and purification of the MS ring

E. coli BL21 (DE3) strain carrying either pKOT112 (ref. ³⁶) (for data set 1) or pKOT105 (ref. ³⁷) (for data set 2) was grown overnight in 20 ml of a cell culture medium containing 0.1 g tryptone, 0.05 g yeast extract, 0.05 g NaCl, 50 μ g/ml of ampicillin and 30 μ g/ml of chloramphenicol in a shaker at 37°C. A 20 ml of overnight culture was added to a 2 l of a cell culture medium containing 10 g tryptone, 5 g yeast extract, 5 g NaCl, 50 μ g/ml of ampicillin and 30 μ g/ml of chloramphenicol and the cells were grown in a 37°C orbital shaker (100 rpm) until the culture density reached an OD₆₀₀ of 0.5~0.7. An aliquot of 0.5 M isopropyl β -D-1-thiogalactopyranoside (IPTG) was added to 2 L cell culture medium to a final concentration of 0.5 mM, and the growth was continued in a 30°C orbital shaker (100 rpm) for 4 h. The cells were collected by centrifugation at 4,600 \times g for 10 min at 4°C. Harvested cells were resuspended in 40 ml of a French press buffer (50 mM Tris-HCl pH 8.0, 5 mM EDTA-NaOH, 50 mM NaCl) containing a protease inhibitor cocktail (Complete, EDTA-free) and were disrupted using a French press at a pressure level of 10,000 psi. After cell debris and

undisrupted cells were removed by centrifugation ($20,000 \times g$, 20 min, 4°C), the crude membrane fraction was isolated by ultracentrifugation ($90,000 \times g$, 60 min, 4°C). The pellet was solubilized in 40 ml of Alkaline buffer (50 mM CAPS-NaOH pH 11.0, 5 mM EDTA-NaOH, 50 mM NaCl, 1% TritonX-100) by mechanical shearing with a 1 ml plastic syringe with 20 gauge needle and was incubated at 4°C for 1 h. After insoluble material was removed by centrifugation ($20,000 \times g$, 20 min, 4°C), solubilized proteins were collected by ultracentrifugation ($90,000 \times g$, 60 min, 4°C). The pellet was resuspended in 3 ml of Buffer S containing 0.1% Triton X-100 by mechanical shearing as above, and the sample was loaded onto a 15-40% (w/w) continuous sucrose density gradient in Buffer C (10 mM Tris-HCl pH 8.0, 5 mM EDTA-NaOH, 1% TritonX-100) and spun by centrifugation in a swing rotor ($49,100 \times g$, 13 h, 4°C). Density fractions with a volume of 700 μl each were collected by a gradient fractionator (BIOCOMP, NB, Canada) and a fraction collector and analyzed by SDS-PAGE for a band of FliF. Peak fractions were collected, and the MS ring was further concentrated by ultracentrifugation ($90,000 \times g$, 60 min, 4°C). The pellet was resuspended in 30 μl of Buffer S containing 0.05% LMNG.

Sample vitrification and cryoEM data acquisition

For the basal body sample, Quantifoil Mo 200 mesh R0.6/1.0 holey carbon grids (Quantifoil) were glow discharged on a glass slide for 10 sec. A 2.5 μL aliquot of the sample solution was applied to the grid and blotted by a filter paper for $3 \text{ s} \times 2$ times with 2 sec drain time at 100% humidity and 4°C . For the MS ring sample, Quantifoil Cu 200 mesh R0.6/1.0 holey carbon grids were glow discharged on a glass slide for 30 sec. A 2.6 μl aliquot of the sample solution was applied onto the grid and blotted by a filter paper for 7 sec at 100% humidity and 4°C . The grids were quickly frozen by rapidly plunging into liquid ethane using a Vitrobot Mark III quick freezing device (Thermo Fisher Scientific). The grids were inserted into a Titan Krios transmission electron microscope (Thermo Fisher Scientific) operated at 300 kV, with the cryo specimen stage cooled with liquid nitrogen. CryoEM images were recorded with a Falcon II $4\text{k} \times 4\text{k}$ CMOS direct electron detector (Thermo Fisher Scientific) at a nominal magnification of $\times 75,000$ for the FliF ring data 1, corresponding to an image pixel size of 1.07 \AA for high-resolution image analysis, or $\times 59,000$ for the FliF ring data 2 and the basal body, corresponding to an image pixel size of 1.4 \AA (Extended Data Table 2), using the EPU software package (Thermo Fisher Scientific). Movie frames were recorded at a dose rate of 45 $\text{e}^{-}/\text{pix}/\text{sec}$ over an exposure time of 2 sec. The total accumulated dose of 90 $\text{e}^{-}/\text{\AA}^2$ was

fractionated into 7 frames. Image data sets of 1,589 (data set 1) and 806 micrographs (data set 2) were collected for the FliF ring, and 1,589 (for 2D classification) and 18,256 (for 3D reconstruction) micrographs for the basal body, using a defocus range between 1.0 and 3.0 μm .

Symmetry analysis of the MS ring of the basal body

Many of the basal body particles in cryoEM images showed end-on views. The particle images were picked up using an in-house particle picking program applying a deep learning method based on YOLO neural network³⁸. About 2,000 particles were manually picked from 200 micrographs and were used for a training of the neural network. In total 34,896 particles were extracted from 1,578 micrographs. 2D classifications were carried out using Relion-2.1 (ref. ³⁹). After 2nd 2D classification, class average images showing the rivet-like structure with the MS ring and the rod were used for rotational symmetry analysis of the MS ring. The outer part of the ring images was converted from Cartesian to polar coordinates, the autocorrelation function was calculated, and the rotational symmetry was analyzed by Fourier transformation (Extended Data Fig. 1b).

3D reconstruction of the basal body

The basal body in Buffer I was used for 3D structural analysis of the basal body. The particle images were picked up using an in-house particle picking program as mentioned above. About 2,000 particles were manually picked up from 200 micrographs and were used for training. In total 385,803 particles were extracted from 18,256 micrographs. 2D and 3D classifications and 3D reconstruction were carried out using Relion-2.1 (ref. ³⁹) or Relion-3.0 (ref. ⁴⁰). We used a 3D map of the basal body in a previous study⁴¹ as the initial 3D model. After subtracting the C-ring density, 275,548 good particle images were used to construct 3D images in five classes. The two best 3D classes were individually refined and then merged for the final 3D refinement. The final 3D map was reconstructed using 149,341 particles at a resolution of 6.8 Å.

Symmetry analysis of the C ring

CryoEM images of the wild-type (CCW) and CW mutant basal bodies were collected using a JEM-3200FSC electron cryomicroscope (JEOL) equipped with a liquid-nitrogen cooled specimen stage, an Ω -type energy filter and a field-emission electron gun, operated at an

accelerating voltage of 200 kV. The images were captured by an F415mp CCD camera (TVIPS) at a magnification of 88,800 \times corresponding to a pixel size of 1.69 Å, a defocus range of 1.0–2.5 μ m and an electron dose of 40 e⁻/Å². Defocus and astigmatism of the images were determined using CTFFIND3 (ref. ⁴²). To estimate the symmetry of the C ring, end-on view images of the basal bodies were boxed out by BOXER⁴³. The C ring part of each end-on view image was converted from the Cartesian to polar coordinates, the autocorrelation function was calculated, and the rotational symmetry was analyzed by Fourier transformation (Extended Data Fig. 1c). The end-on view images with distinct rotational symmetries were also classified, aligned and averaged to show the C ring images with different symmetries in Extended Data Fig. 1c.

Image processing of the MS ring formed by overexpressed FliF

Image processing procedures of the MS ring are described in Extended Data Fig. 3 and 7. The movie frames were aligned to correct for beam-induced movement and drift by MotionCor2 (ref. ⁴⁴), and the parameters of the contrast transfer function (CTF) were estimated by Gctf⁴⁵.

For the FliF ring data set 1 with the outer M ring part disordered, in total 339,861 particle images were automatically picked up from 1,589 micrographs using Gautomatch (<http://www.mrc-lmb.cam.ac.uk/kzhang/>), and then 2D and 3D classifications were performed using Relion-2.1 (ref. ³⁹) and 3.0 (ref. ⁴⁰). Particle images from good 2D class average images were selected for the initial 3D model using CryoSPARC2 (ref. ⁴⁶). In total, 99,560 particles from the best 3D class were subjected to ab initio reconstruction and hetero refinement, and finally 38,889 particles from the best hetero refinement model were subjected to non-uniform refinement with C34 rotational symmetry using CryoSPARC2 (ref. ⁴⁶). The final refinement yielded a 3D map with a global resolution of 3.70 Å and a B factor of -197.5 Å² according to 0.143 criterion of the Fourier shell correlation (FSC). The local resolution was estimated using CryoSPARC2 (ref. ⁴⁶). The processing strategy is described in Extended Data Fig. 3, and the model refinement statistics in Extended Data Table 2.

For the FliF ring data set 2 with the M ring part well ordered, in total 156,459 particle images were automatically picked from 806 micrographs using Gautomatch (<http://www.mrc-lmb.cam.ac.uk/kzhang/>), and 2D and 3D classifications were performed using Relion-2.1 (ref. ³⁹). Particle images from good 2D class average images were selected for the initial 3D model using CryoSPARC2 (ref. ⁴⁶). In total, 18,883 particles from the best 3D class were subjected to 3D refinement with C1, C11 and C34 rotational symmetry using Relion-2.1 (ref. ³⁹). The final refinement and postprocessing yielded a 3D map with a global

resolution and a B-factor of 12 Å and -35 Å² for C1, 9.0 Å and -495 Å² for C11 and 7.4 Å and -450 Å² for C34, according to 0.143 criterion of the FSC. The processing strategy is described in Extended Data Fig. 7, and the model refinement statistics in Extended Data Table 2.

Model building and refinement of the S ring structure

The atomic model of the S ring was constructed using Coot⁴⁷ and refined with real space refinement based on the cryoEM map (EMD-30612) using Phenix⁴⁸ under NCS constraints of 34-fold rotational symmetry and secondary structure restraints. The refinement statistics are summarized in Extended Data Table 2.

Site directed mutagenesis

Site-directed mutagenesis was carried out using the QuickChange site-directed mutagenesis method (Stratagene). All of the *fliF* mutations were confirmed by DNA sequencing. DNA sequencing reactions were carried out using BigDye v3.1 (Applied Biosystems) and then the reaction mixtures were analyzed by a 3130 Genetic Analyzer (Applied Biosystems).

Motility assays

We transformed a *Salmonella fliF* null mutant strain, TH12415 ($\Delta fliF$), with pET22b-based plasmids, and the resulting transformants were inoculated onto soft tryptone agar plates containing 100 µg/ml ampicillin and incubated at 30°C.

Fractionation of cell membrane. *Salmonella* TH12415 cells harbouring an appropriate plasmid were grown exponentially in 30 ml L-broth at 30°C with shaking. The cells were harvested, resuspended in 3 ml PBS, and sonicated. After the cell debris was removed by low-speed centrifugation, the cell lysates were ultracentrifuged (100,000 × g, 60 min, 4°C). After carefully removing the soluble fractions, membranes were resuspended in 300 µl of SDS-loading buffer and heated at 95°C for 3 min. After SDS-PAGE, immunoblotting with polyclonal anti-FliF or anti-FliN antibody was carried out as described previously²⁸. An ECL prime immunoblotting detection kit (GE Healthcare) was used to detect target bands. Chemiluminescence signals were detected by a Luminoimage analyzer, LAS-3000 (GE Healthcare).

Flagellar protein export assay.

Details of sample preparations have been described previously⁴⁹. Both whole cellular proteins and culture supernatants were normalized to a cell density of each culture to give a constant number of *Salmonella* cells. After SDS-PAGE, immunoblotting with polyclonal anti-FlgD, anti-FlgE or anti-FliC antibody was performed.

***in vivo* disulfide crosslinking**

Salmonella TH12415 cells harboring pMMiF001, pMMiF008, pMMiF009 or pMMiF011 were exponentially grown in L-broth containing 100 µg/ml ampicillin at 30°C with shaking. Aliquots of the cultures containing a constant number of cells were centrifuged to harvest the cells. The membrane fraction was prepared as described previously⁵⁰. Disulfide crosslinking were induced by adding iodine as described before⁵¹. After SDS-PAGE using 4–15% Mini-PROTEAN TGX Precast gels (Bio-Rad), immunoblotting with polyclonal anti-FliG antibody was carried out as described previously²⁸.

Data availability

The cryoEM volume has been deposited in the Electron Microscopy Data Bank under accession code EMD-30612, EMD-30613, EMD-30360, EMD-30361, EMD-30363 and the atomic coordinates have been deposited in the Protein Data Bank under accession code 7D84. Other data are available from the corresponding author upon reasonable request.

References

1. Namba, K. & Vonderviszt, F. Molecular architecture of bacterial flagellum. *Q Rev Biophys* **30**, 1-65 (1997).
2. Minamino, T., Imada, K. & Namba, K. Molecular motors of the bacterial flagella. *Curr Opin Struct Biol* **18**, 693-701 (2008).
3. Nakamura, S. & Minamino, T. Flagella-Driven Motility of Bacteria. *Biomolecules* **9**, 279 (2019).
4. Minamino, T. & Imada, K. The bacterial flagellar motor and its structural diversity. *Trends Microbiol* **23**, 267-274 (2015).
5. Okino, H. et al. Release of flagellar filament-hook-rod complex by a *Salmonella typhimurium* mutant defective in the M ring of the basal body. *J Bacteriol* **171**, 2075-2082 (1989).
6. Fujii, T. et al. Identical folds used for distinct mechanical functions of the bacterial flagellar rod and hook. *Nat Commun* **8**, 14276 (2017).
7. Berg, H.C. The rotary motor of bacterial flagella. *Annu Rev Biochem* **72**, 19-54 (2003).

- 570 8. Minamino, T., Terahara, N., Kojima, S. & Namba, K. Autonomous control mechanism
571 of stator assembly in the bacterial flagellar motor in response to changes in the
572 environment. *Mol Microbiol* **109**, 723-734 (2018).
- 573 9. Jones, C.J., Macnab, R.M., Okino, H. & Aizawa, S. Stoichiometric analysis of the
574 flagellar hook-(basal-body) complex of *Salmonella typhimurium*. *J Mol Biol* **212**,
575 377-387 (1990).
- 576 10. Suzuki, H., Yonekura, K. & Namba, K. Structure of the rotor of the bacterial flagellar
577 motor revealed by electron cryomicroscopy and single-particle image analysis. *J Mol*
578 *Biol* **337**, 105-113 (2004).
- 579 11. Thomas, D.R., Morgan, D.G. & DeRosier, D.J. Rotational symmetry of the C ring and
580 a mechanism for the flagellar rotary motor. *Proc Natl Acad Sci U S A* **96**, 10134-10139
581 (1999).
- 582 12. Thomas, D.R., Francis, N.R., Xu, C. & DeRosier, D.J. The three-dimensional structure
583 of the flagellar rotor from a clockwise-locked mutant of *Salmonella enterica* serovar
584 Typhimurium. *J Bacteriol* **188**, 7039-7048 (2006).
- 585 13. Sakai, T. et al. Novel Insights into Conformational Rearrangements of the Bacterial
586 Flagellar Switch Complex. *mBio* **10**, e00079-19 (2019).
- 587 14. Sowa, Y. et al. Direct observation of steps in rotation of the bacterial flagellar motor.
588 *Nature* **437**, 916-919 (2005).
- 589 15. Nakamura, S., Kami-ike, N., Yokota, J.P., Minamino, T. & Namba, K. Evidence for
590 symmetry in the elementary process of bidirectional torque generation by the bacterial
591 flagellar motor. *Proc Natl Acad Sci U S A* **107**, 17616-17620 (2010).
- 592 16. Johnson, S. et al. Symmetry mismatch in the MS-ring of the bacterial flagellar rotor
593 explains the structural coordination of secretion and rotation. *Nat Microbiol* **5**,
594 966-975 (2020).
- 595 17. Young, H.S., Dang, H., Lai, Y., DeRosier, D.J. & Khan, S. Variable symmetry in
596 *Salmonella typhimurium* flagellar motors. *Biophys J* **84**, 571-577 (2003).
- 597 18. Fukumura, T. et al. Assembly and stoichiometry of the core structure of the bacterial
598 flagellar type III export gate complex. *PLoS Biol* **15**, e2002281 (2017).
- 599 19. Kuhlen, L. et al. Structure of the core of the type III secretion system export apparatus.
600 *Nat Struct Mol Biol* **25**, 583-590 (2018).
- 601 20. Tomoyasu, T. et al. The ClpXP ATP-dependent protease regulates flagellum synthesis
602 in *Salmonella enterica* serovar Typhimurium. *J Bacteriol* **184**, 645-653 (2002).
- 603 21. Zeytuni, N. et al. Near-atomic resolution cryoelectron microscopy structure of the
604 30-fold homooligomeric SpoIIAG channel essential to spore formation in *Bacillus*
605 *subtilis*. *Proc Natl Acad Sci U S A* **114**, E7073-E7081 (2017).
- 606 22. Yip, C.K. et al. Structural characterization of the molecular platform for type III
607 secretion system assembly. *Nature* **435**, 702-707 (2005).

23. Levдикov, V.M. et al. Structure of components of an intercellular channel complex in sporulating *Bacillus subtilis*. *Proc Natl Acad Sci U S A* **109**, 5441-5445 (2012).
24. Meisner, J., Maehigashi, T., André, I., Dunham, C.M. & Moran, C.P., Jr. Structure of the basal components of a bacterial transporter. *Proc Natl Acad Sci U S A* **109**, 5446-5451 (2012).
25. Bergeron, J.R. et al. A refined model of the prototypical *Salmonella* SPI-1 T3SS basal body reveals the molecular basis for its assembly. *PLoS Pathog* **9**, e1003307 (2013).
26. Bergeron, J.R.C. et al. The modular structure of the inner-membrane ring component PrgK facilitates assembly of the type III secretion system basal body. *Structure* **23**, 161-172 (2015).
27. Worrall, L.J. et al. Near-atomic-resolution cryo-EM analysis of the *Salmonella* T3S injectisome basal body. *Nature* **540**, 597-601 (2016).
28. Minamino, T. & Macnab, R.M. Components of the *Salmonella* flagellar export apparatus and classification of export substrates. *J Bacteriol* **181**, 1388-1394 (1999).
29. Kihara, M., Minamino, T., Yamaguchi, S. & Macnab, R.M. Intergenic suppression between the flagellar MS ring protein FliF of *Salmonella* and FlhA, a membrane component of its export apparatus. *J Bacteriol* **183**, 1655-1662 (2001).
30. Kuhlen, L. et al. The substrate specificity switch FlhB assembles onto the export gate to regulate type three secretion. *Nat Commun* **11**, 1296 (2020).
31. Lynch, M.J. et al. Co-Folding of a FliF-FliG Split Domain Forms the Basis of the MS:C Ring Interface within the Bacterial Flagellar Motor. *Structure* **25**, 317-328 (2017).
32. Xue, C. et al. Crystal structure of the FliF-FliG complex from *Helicobacter pylori* yields insight into the assembly of the motor MS-C ring in the bacterial flagellum. *J Biol Chem* **293**, 2066-2078 (2018).
33. Francis, N.R., Irikura, V.M., Yamaguchi, S., DeRosier, D.J. & Macnab, R.M. Localization of the *Salmonella typhimurium* flagellar switch protein FliG to the cytoplasmic M-ring face of the basal body. *Proc Natl Acad Sci U S A* **89**, 6304-6308 (1992).
34. Minamino, T. & MacNab, R.M. Interactions among components of the *Salmonella* flagellar export apparatus and its substrates. *Mol Microbiol* **35**, 1052-1064 (2000).
35. Togashi, F., Yamaguchi, S., Kihara, M., Aizawa, S.I. & Macnab, R.M. An extreme clockwise switch bias mutation in fliG of *Salmonella typhimurium* and its suppression by slow-motile mutations in motA and motB. *J Bacteriol* **179**, 2994-3003 (1997).
36. Ueno, T., Oosawa, K. & Aizawa, S. Domain structures of the MS ring component protein (FliF) of the flagellar basal body of *Salmonella typhimurium*. *J Mol Biol* **236**, 546-555 (1994).
37. Ueno, T., Oosawa, K. & Aizawa, S. M ring, S ring and proximal rod of the flagellar

- basal body of *Salmonella typhimurium* are composed of subunits of a single protein, FliF. *J Mol Biol* **227**, 672-677 (1992).
38. Redmon, J., Divvala, S., Girshick, R. & Farhadi, A. You only look once: unified, real-time object detection. *Proceedings of the IEEE Conference on Computer Vision and Pattern Recognition (CVPR)*, 779-788 (2016).
39. Kimanius, D., Forsberg, B.O., Scheres, S.H. & Lindahl, E. Accelerated cryo-EM structure determination with parallelisation using GPUs in RELION-2. *Elife* **5**, e18722 (2016).
40. Zivanov, J. et al. New tools for automated high-resolution cryo-EM structure determination in RELION-3. *Elife* **7**, e42166 (2018).
41. Kawamoto, A. et al. Common and distinct structural features of *Salmonella* injectisome and flagellar basal body. *Sci Rep* **3**, 3369 (2013).
42. Mindell, J.A. & Grigorieff, N. Accurate determination of local defocus and specimen tilt in electron microscopy. *Journal of Structural Biology* **142**, 334-347 (2003).
43. Ludtke, S.J., Baldwin, P.R. & Chiu, W. EMAN: semiautomated software for high-resolution single-particle reconstructions. *J Struct Biol* **128**, 82-97 (1999).
44. Zheng, S.Q. et al. MotionCor2: anisotropic correction of beam-induced motion for improved cryo-electron microscopy. *Nat Methods* **14**, 331-332 (2017).
45. Zhang, K. Gctf: Real-time CTF determination and correction. *J Struct Biol* **193**, 1-12 (2016).
46. Punjani, A., Rubinstein, J.L., Fleet, D.J. & Brubaker, M.A. cryoSPARC: algorithms for rapid unsupervised cryo-EM structure determination. *Nat Methods* **14**, 290-296 (2017).
47. Emsley, P., Lohkamp, B., Scott, W.G. & Cowtan, K. Features and development of Coot. *Acta Crystallogr D Biol Crystallogr* **66**, 486-501 (2010).
48. Adams, P.D. et al. PHENIX: a comprehensive Python-based system for macromolecular structure solution. *Acta Crystallogr D Biol Crystallogr* **66**, 213-221 (2010).
49. Minamino, T., Kinoshita, M. & Namba, K. Fuel of the Bacterial Flagellar Type III Protein Export Apparatus. *Methods Mol Biol* **1593**, 3-16 (2017).
50. Baker, M.A. et al. Domain-swap polymerization drives the self-assembly of the bacterial flagellar motor. *Nat Struct Mol Biol* **23**, 197-203 (2016).
51. Hara, N., Morimoto, Y.V., Kawamoto, A., Namba, K. & Minamino, T. Interaction of the extreme N-terminal region of FliH with FlhA is required for efficient bacterial flagellar protein export. *J Bacteriol* **194**, 5353-5360 (2012).

Acknowledgements

We thank Kelly T. Hughes for his kind gift of a *Salmonella fliF* null mutant, Tomoko Yamamoto for a phage for *clpP* deletion, Hideyuki Matsunami for *Salmonella* HK1003 mutant strain and Noriyuki Takekawa for help preparing a figure. This research was supported in part by JSPS KAKENHI Grant Numbers 25000013 to K.N, 18K06155 and 20770083 to T.Miyata, 18K14639 to A.K, JP26293097 and JP19H03182 to T.Minamino, JP15H05593 and JP20K15749 to M.K., JP15H02386 to K.I., and MEXT KAKENHI Grant Numbers JP15H01640 to T.Minamino. This research was also supported by Platform Project for Supporting Drug Discovery and Life Science Research (BINDS) from AMED under Grant Number JP19am0101117 to K.N., by the Cyclic Innovation for Clinical Empowerment (CiCLE) Grant Number JP17pc0101020 from AMED to K.N. and by JEOL YOKOGUSHI Research Alliance Laboratories of Osaka University to K.N.

Author contributions

T.K. and K.N. conceived the project; A.K., T.K., T.Minamino and K.N. designed experiments; A.K. and T.Miyata prepared the sample for cryoEM; T.K. set up cryoEM imaging system including both hardware and software; A.K., T. Miyata, F.M. and T.K. collected and analyzed cryoEM image data; M.K. and T.Minamino performed genetic, biochemical and physiological experiments; A.K. and K.I. built the atomic model; All authors studied the atomic model; A.K., T.Miyata, T.Minamino, K.I, T.K. and K.N wrote the paper based on discussion with the other authors.

Competing interests

The authors declare no competing interests.

Additional information

Extended Data is available for this paper at

Correspondence and requests for materials should be addressed to T.K. and K.N.

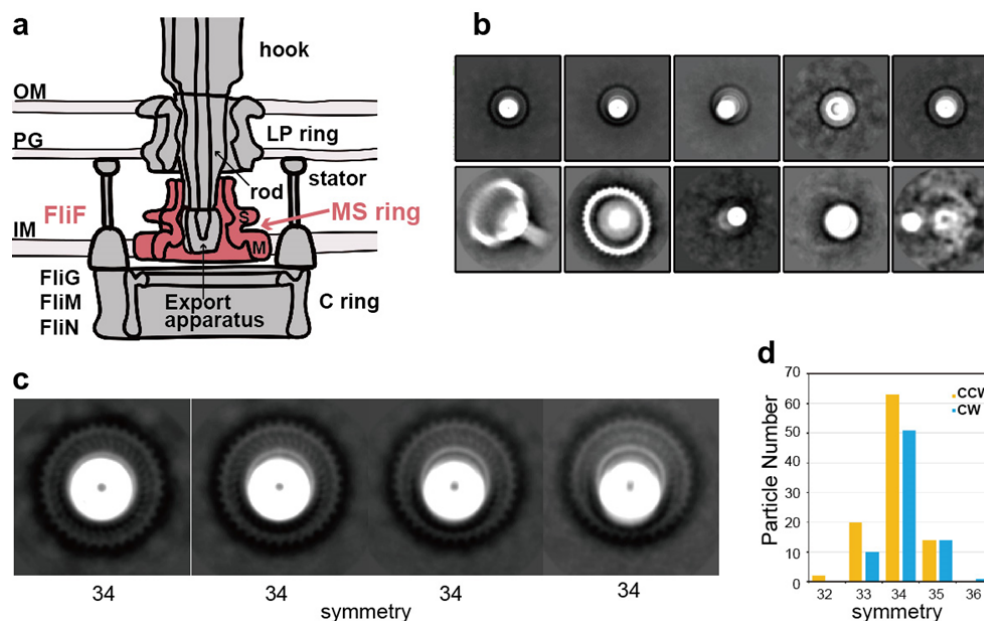


Fig. 1 Schematic diagram and cryoEM image analysis of the flagellar basal body. **a**, Schematic diagram of the flagellar basal body. IM: inner membrane; PG: peptidoglycan layer; OM: outer membrane. **b**, Representative 2D class average images in the first round. The upper row images show end-on views of the MS ring with rod called rivet (see Extended Data Fig. 1a) except for the second from the right; in the lower row, the two panels on the left show the rivet with the C ring attached. **c**, Images showing the rotational symmetry of the S ring are extracted from the second round of 2D class average of the rivet class images and magnified. The rotational symmetries obtained by image analysis as shown in Extended Data Fig. 1 are indicated below, presenting direct evidence for the 34-fold symmetry of the native MS ring. **d**, The rotational symmetry distributions of the C ring: CCW in yellow is the wild-type motor in the CCW state (98 particles in total); and CW in blue is the CW-locked motor by FliG Δ PAA mutation (75 particles in total).

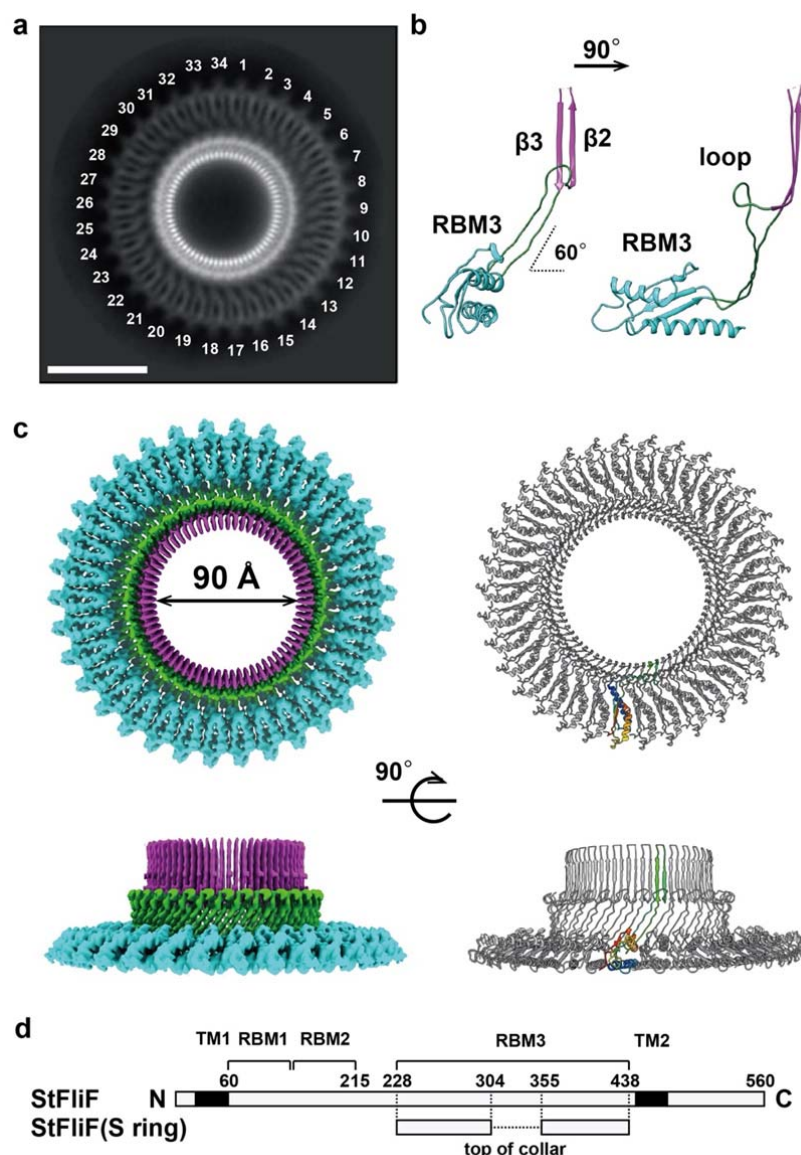


Fig. 2 Structure of the S ring and collar of the MS ring formed by full-length FliF. a, Representative 2D class average images. **b,** C α ribbon representation of the RBM3 domain model forming the S ring and collar in two orthogonal side views. **c,** CryoEM 3D image reconstruction of the S ring and collar (left) and C α ribbon diagram of the atomic model (right) in end-on (upper) and side (lower) views. **d,** Domain organization of *Salmonella* FliF, indicating the region forming the S ring and collar. TM1 and TM2: transmembrane regions; numbers above the bars: residue numbers in the FliF sequence.

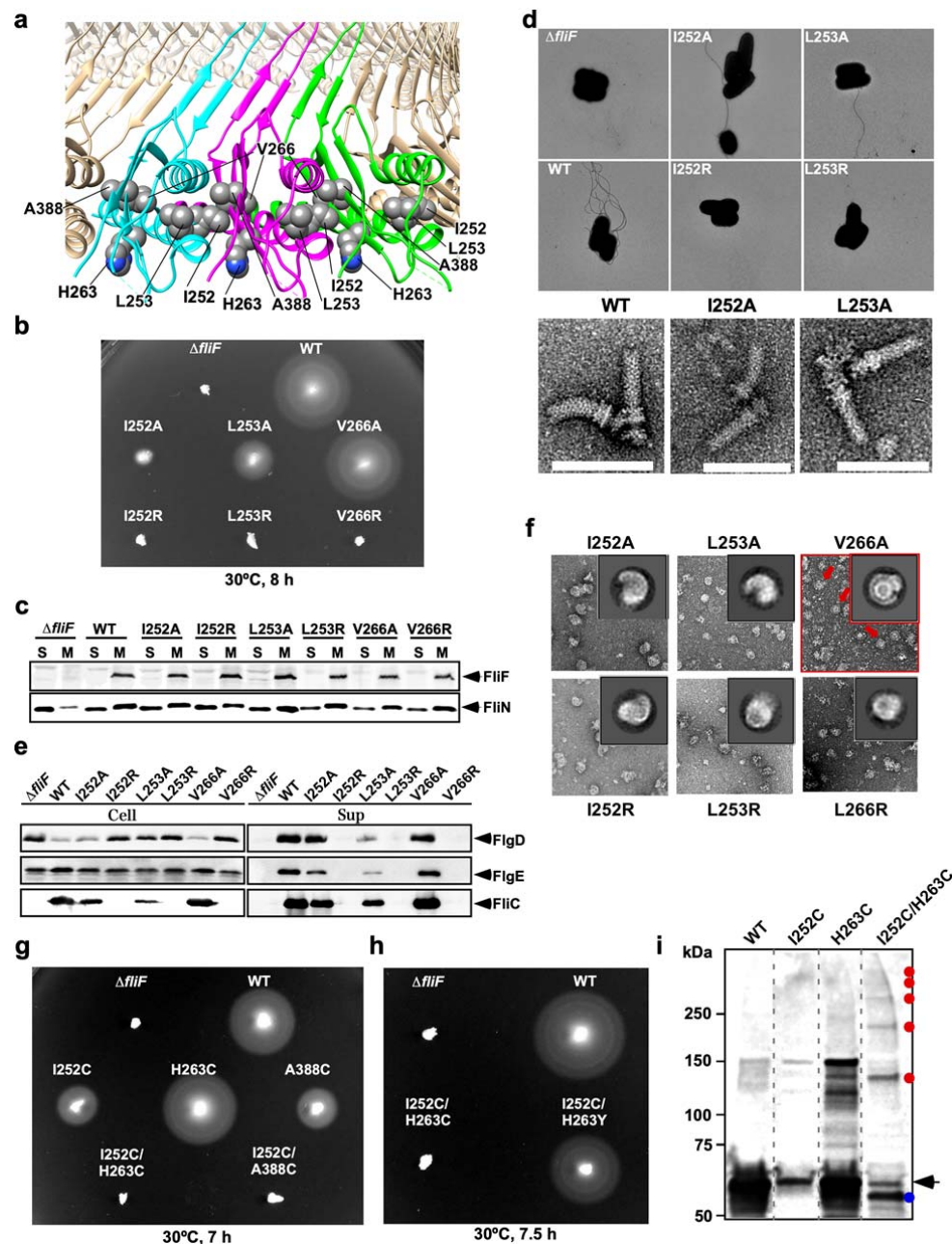


Fig. 3. Mutational analysis of conserved Ile-252, Leu-253 and Val-266. **a**, Molecular interface between FliF subunits. Ile-252, Leu-253 and Val-266 residues are located at an interface between FliF subunits. His-263 and Ala-388 are in close proximity to Ile-252. **b**, Motility assay of *Salmonella* TH12415 cells harboring pET3c ($\Delta fliF$), pMMiF001 (WT), pMMiF002 (I252A), pMMiF003 (I252R), pMMiF004 (L253A), pMMiF005 (L253R), pMMiF006 (V266A) or pMMiF007 (V266R) in soft agar. The plate was incubated at 30 °C for 8 hours. **c**, Membrane localization of the MS ring protein FliF and the C ring protein FliN. The membrane fractions of the above transformants were prepared after sonication and ultracentrifugation. Then, the membrane fractions were subjected to SDS-PAGE and analyzed by immunoblotting with polyclonal anti-FliF or anti-FliN antibody. Positions of FliF and FliN are indicated by

arrow heads. **d**, Electron micrographs of cells of TH12415 cells harboring pET3c ($\Delta fliF$), pMMiF001 (WT), pMMiF002 (I252A), pMMiF003 (I252R), pMMiF004 (L253A) or pMMiF005 (L253R) and purified hook-basal bodies isolated from WT, I252A and L253A cells. **e**, Secretion assays. Whole cell proteins (Cell) and culture supernatant fractions (Sup) were prepared from the above strains. An 8 μ l solution of each protein sample, which was normalized to an optical density of OD₆₀₀, was subjected to SDS-PAGE, followed by immunoblotting with polyclonal anti-FlgD (first row), anti-FlgE (second row) or anti-FliC (third row) antibody. **f**, Negative-stain EM images of the MS rings isolated from the six FliF mutants. **g**, Motility assay of *Salmonella* TH12415 cells harboring pET3c ($\Delta fliF$), pMMiF001 (WT), pMMiF008 (I252C), pMMiF009 (H263C), pMMiF010 (A388C), pMMiF011 (I252C/H263C) or pMMiF012 (I252C/A388C) in soft agar. The plate was incubated at 30 °C for 7 hours. **h**, Isolation of pseudorevertants from the I252C/H263C mutant cells. Motility assay of *Salmonella* TH12415 cells harboring pET3c ($\Delta fliF$), pMMiF001 (WT), pMMiF008 (I252C), pMMiF011 (I252C/H263C) or pMMiF011SP-1 (I252C/H263Y) in soft agar. The plate was incubated at 30 °C for 7.5 hours. **i**, Disulfide crosslinking of FliF–FliF interface. The membrane fractions were prepared from TH12415 cells expressing wild-type FliF FliF(I252C), FliF(H263C) or FliF(I252C/H263C), and disulfide crosslinking were induced by adding iodine. Then, each sample, which was normalized to an optical density of OD₆₀₀, was treated with N-ethylmaleimide, followed by non-reducing SDS-PAGE with a 4–15% gradient SDS-gel and finally immunoblotting with polyclonal anti-FliF antibody. Oligomeric and monomeric forms are indicated by red dots and an arrow, respectively. A blue dot presumably indicates FliF monomers with an intramolecular disulfide bond. Molecular mass markers are shown on the left.

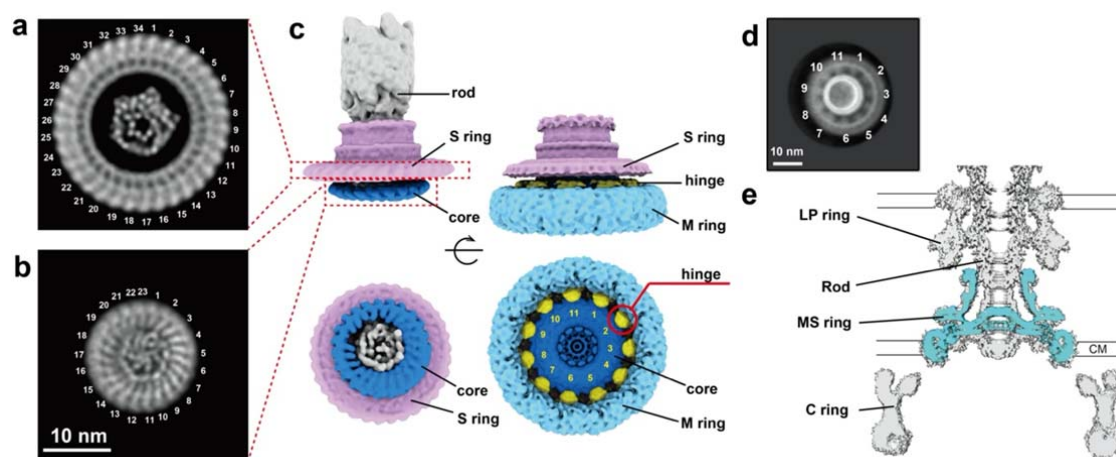
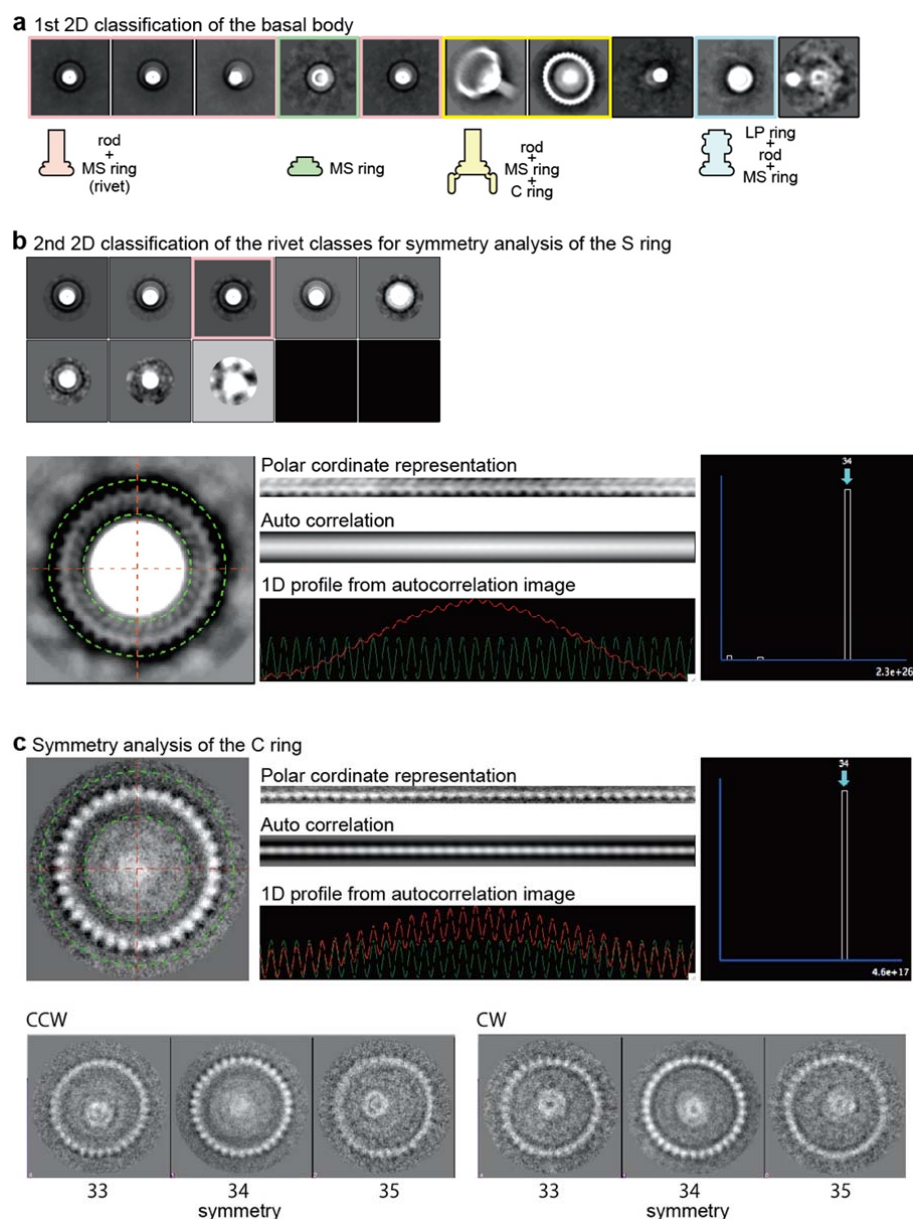


Fig. 4 CryoEM structure of the 34-subunits MS ring with 23-fold and 11-fold subsymmetries. a, b, End-on views of the S ring (a) and inner part of the M ring (b) of the basal body, showing the 34-fold and 23-fold rotational symmetries, respectively. The dot- and rod-like densities at the center of the rings represent the structure of the type III protein export gate formed by FliP, FliQ and FliR. **c,** 3D reconstructions of the basal body (left) and the MS ring formed by full-length FliF (right) in side (upper) and end-on (lower) views. **d,** 2D class average image of the MS ring in end-on view, revealing the 11-fold rotational symmetry in the M ring. **e,** A central section of the MS ring density through the axis (blue) is well superimposed on that of the basal body density, indicating the structural identity of the MS ring formed by full-length FliF with that of the basal body.

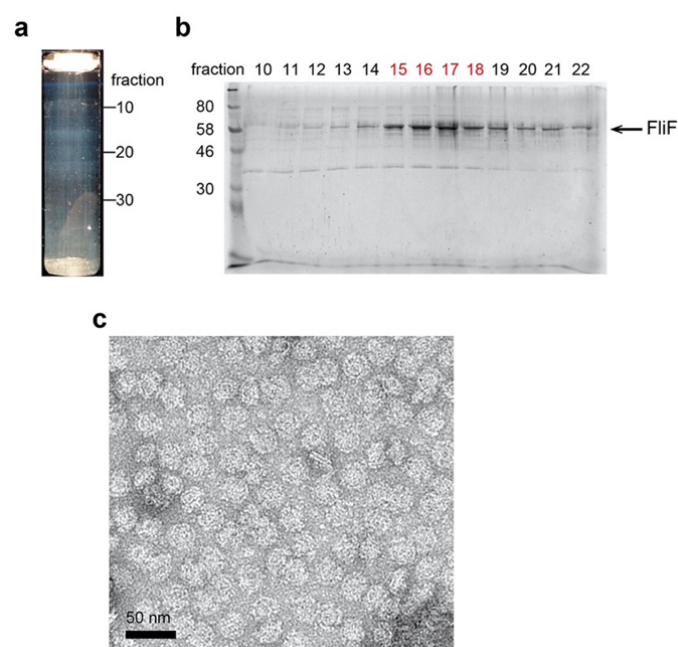
Extended Data

**Native structure of flagellar MS ring is formed by 34 subunits with
23-fold and 11-fold subsymmetries**

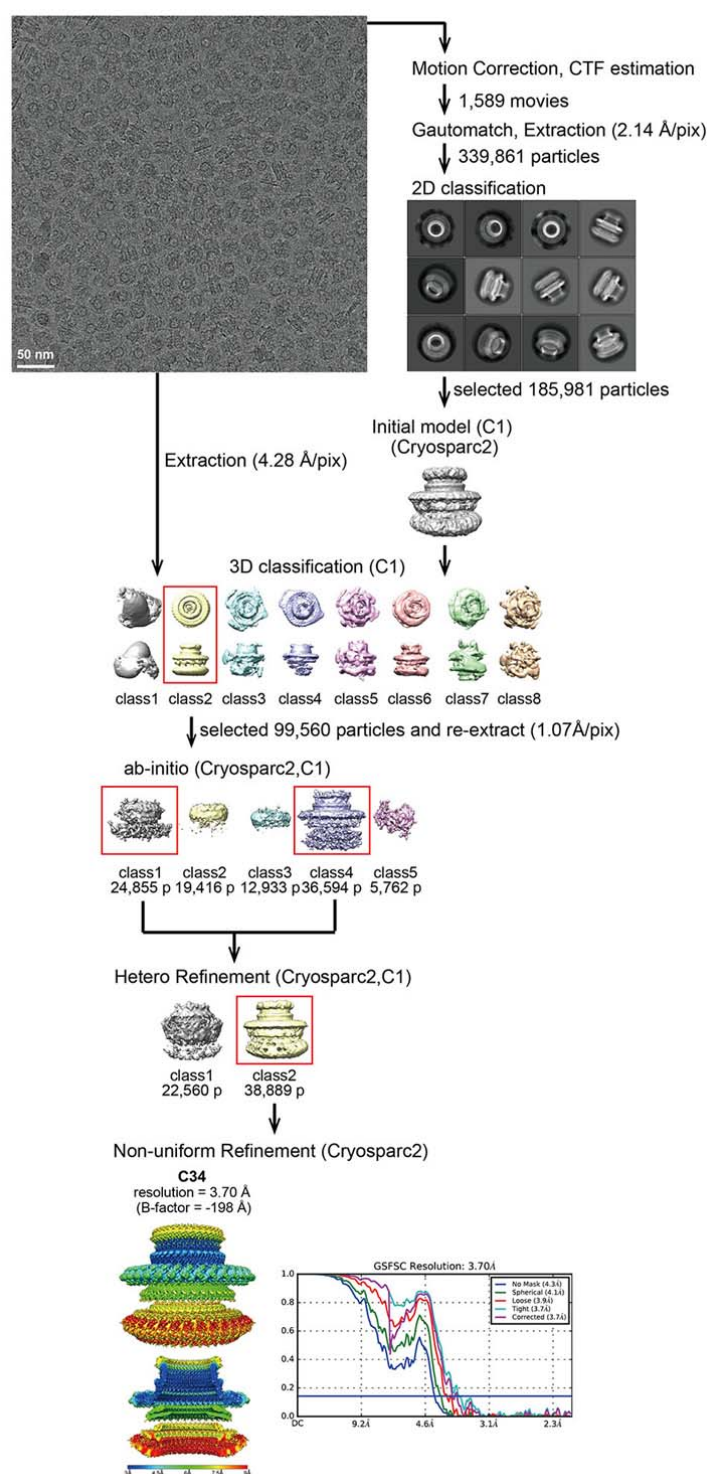
**Akihiro Kawamoto, Tomoko Miyata, Fumiaki Makino, Miki Kinoshita, Tohru
Minamino, Katsumi Imada, Takayuki Kato and Keiichi Namba**



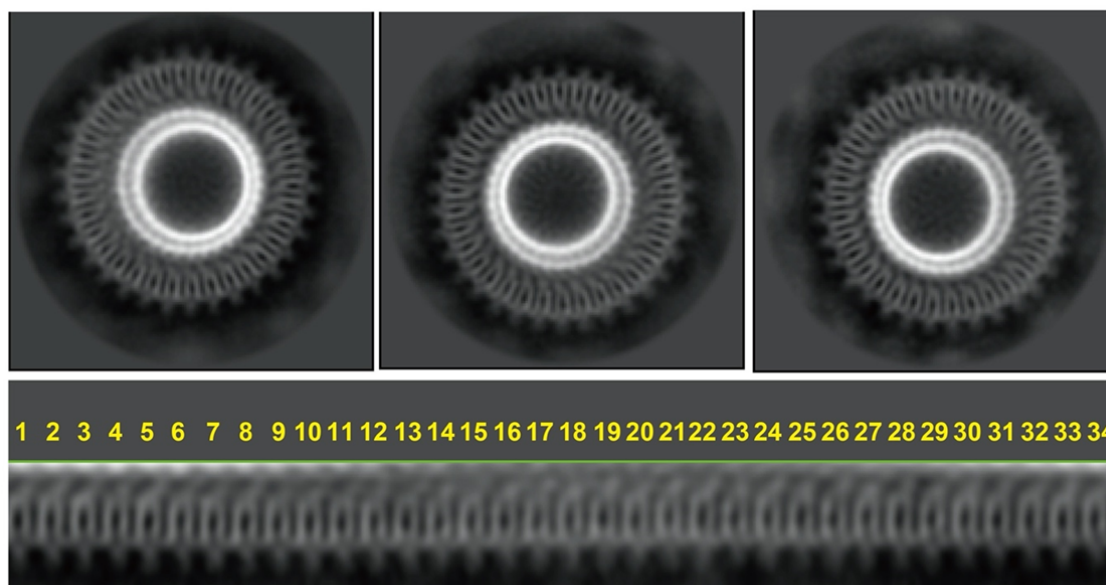
Extended Data Fig. 1 CryoEM single particle 2D Image analyses of the basal body M ring and C ring. **a**, 2D class average images of the basal body in the first round with identification of the types of substructures schematically depicted below. **b**, The upper panel shows the second round 2D class average for the images of the rivet class (pink boxes in **a**). The rotational symmetry of the S ring was analyzed by image analysis described in the lower panels. **c**, Symmetry analysis of the C ring with end-on view images. The upper panel describes how the image analysis is done, and the lower panels show C ring images of different rotational symmetries. WT: the wild-type motor in the CCW state; and CW: the CW-locked motor by FliG Δ PAA mutation³⁵. The image presented here are averages of many particles for easy recognition of their symmetries, but the actual symmetry analysis was done with individual particle images used in a previous study¹³.



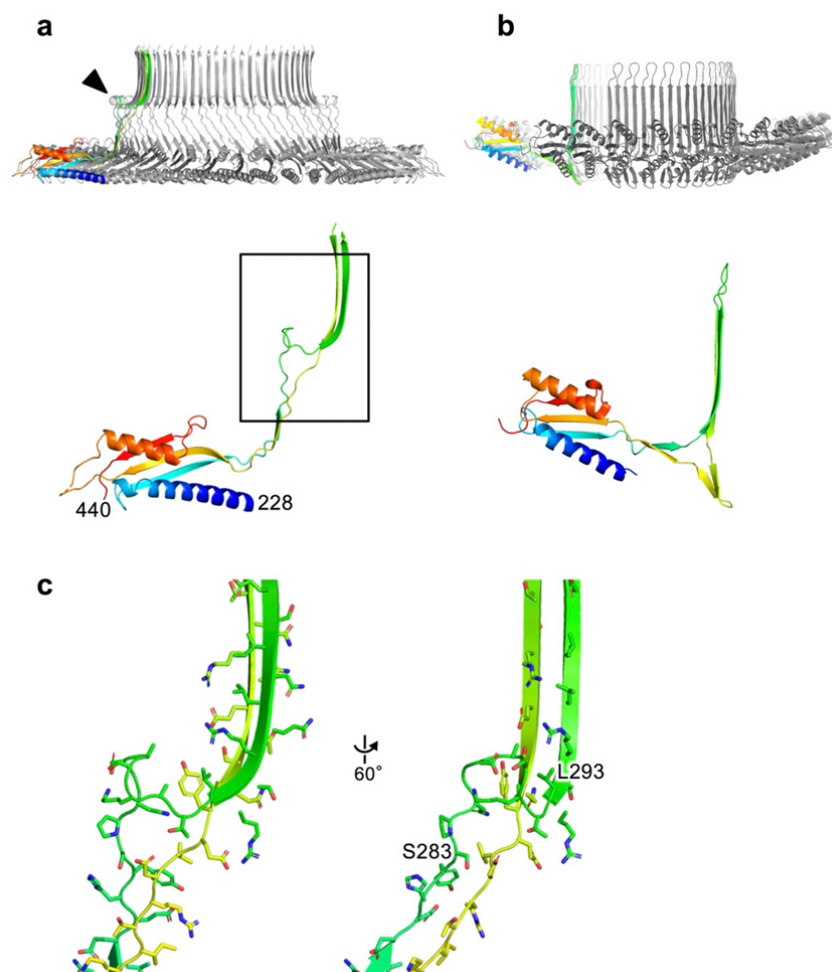
Extended Data Fig. 2 Purification of the MS ring formed by full-length FliF. **a**, The sucrose gradient for purification of the MS ring with fraction numbers on the right. **b**, SDS-PAGE band pattern of each fraction of the sucrose gradient shown in **a**. **c**, Negative-stain EM image of the purified MS rings.



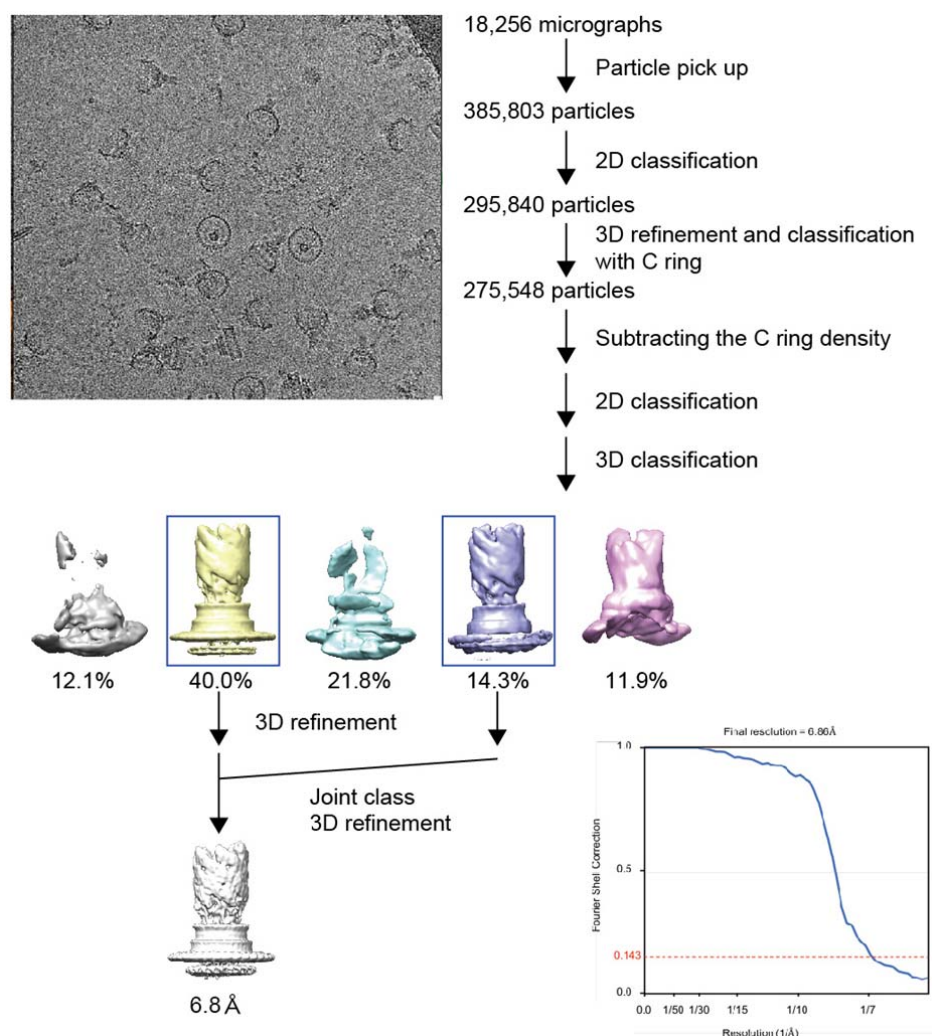
Extended Data Fig. 3 CryoEM single particle 3D image analysis of the MS ring formed by FliF expressed from a plasmid pKOT112(ref. ³⁶) (data set 1).



Extended Data Fig. 4 CryoEM single particle 2D image analyses of the MS ring. Upper three panels show 2D class average images of the MS ring in end-on views with slightly different orientation, which all clearly indicate 34-fold rotational symmetry of the S ring and collar, as analyzed by converting the images into the polar coordinates as shown in the lower panel.

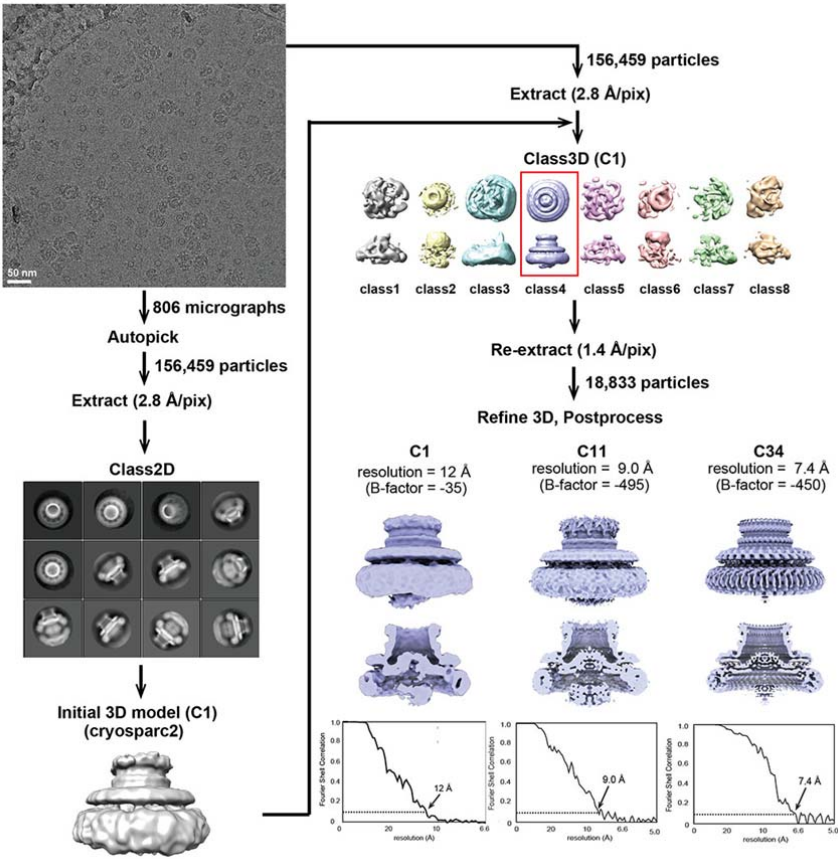


Extended Data Fig. 5 Structural comparison of the S ring and SpoIIAG. **a**, the S ring; **b**, SpoIIAG (PDB ID: 5WC3) in C α ribbon representation with rainbow color according to the sequence from the N-terminus in blue to the C-terminus in red. **c**, Magnified views of part of FliF forming the collar above the S ring, as indicated by the square box in **a**.



Extended Data Fig. 6 CryoEM single particle 3D image analysis of the flagellar basal body focusing on the MS ring and rod.

828



829

830

831 **Extended Data Fig. 7 CryoEM single particle 3D image analysis of the MS ring formed**
832 **by FliF expressed from a plasmid pKOT105 (ref. ³⁷) (data set 2).**

833

834 **Extended Data Table 1. Strains and plasmids used in this study**

Strains and Plasmids	Relevant characteristics	Source or reference
<i>Escherichia coli</i>		
BL21 Star (DE3)	Over-expression of wild-type FliF and its mutant variants	Novagen
<i>Salmonella</i>		
TH12415	$\Delta fliF7355$	Kelly. T. Hughes
HK1003	$flgE\Delta(9-20) \Delta clpP::Cm$	Hideyuki Matsunami
TM022	$flgE\Delta(9-20) \Delta clpP::Cm fliG\Delta PAA$	Ref. 13
Plasmids		
pKOT105	pET3b / FliF	Ref. 37
pKOT112*	pET3b / FliF	Ref. 36
pET3c	Expression vector	GE Healthcare
pMMiF001	pET3c / FliF	This study
pMMiF001TH	pET3c / FliF-TEV-His ₁₀	This study
pMMiF002	pET3c / FliF(I252A)	This study
pMMiF00TH	pET3c / FliF(I252A)-TEV-His ₁₀	This study
pMMiF003	pET3c / FliF(I252R)	This study
pMMiF003TH	pET3c / FliF(I252R)-TEV-His ₁₀	This study
pMMiF004	pET3c / FliF(L253A)	This study
pMMiF004TH	pET3c / FliF(L253A)-TEV-His ₁₀	This study
pMMiF005	pET3c / FliF(L253R)	This study
pMMiF005TH	pET3c / FliF(L253R)-TEV-His ₁₀	This study
pMMiF006	pET3c / FliF(V266A)	This study
pMMiF006TH	pET3c / FliF(V266A)-TEV-His ₁₀	This study
pMMiF007	pET3c / FliF(V266R)	This study
pMMiF007TH	pET3c / FliF(V266R)-TEV-His ₁₀	This study
pMMiF008	pET3c / FliF(I252C)	This study
pMMiF009	pET3c / FliF(H263C)	This study
pMMiF0010	pET3c / FliF(A388C)	This study
pMMiF011	pET3c / FliF(I252C/H263C)	This study
pMMiF011SP-1	pET3c / FliF(I252C/H263Y)	This study
pMMiF012	pET3c / FliF(I252C/A388C)	This study

835 *pKOT112 was supposed to contain a sequence corresponding to a C-terminally truncated FliF
836 fragment (Ser-1 to Asp-456) but the plasmid we received actually contained full-length FliF.

837

838 **Extended Data Table 2 CryoEM data collection, refinement and validation statistics**

	#1 FliF ring (data1) (EMDB-30612) (PDB 7D84)	#2 FliF ring (data2) (EMDB-30363, EMDB-30360) EMDB-30361,			#3 basal body (EMDB-30613)
Data collection and processing					
Magnification	75,000	59,000			59,000
Voltage (kV)	300	300			300
Electron exposure (e-/Å ²)	90	90			90
Defocus range (μm)	1.0-3.0	1.0-3.0			0.5-3.5
Pixel size (Å)	1.07	1.4			1.4
Symmetry imposed	34	1	11	34	1
Initial particle images (no.)	339,861	156,459			385,803
Final particle images (no.)	38,889	18,833			149,341
Map resolution (Å)	3.70	12.0	9.0	7.4	6.8
FSC threshold	0.143	0.143	0.143	0.143	0.143
Map resolution range (Å)	3.0-9.0				
Refinement					
Initial model used (PDB code)	-				
Model resolution (Å)	4.2				
FSC threshold	0.5				
Model resolution range (Å)	3.7-4.2				
Map sharpening <i>B</i> factor (Å ²)					
Model composition					
Non-hydrogen atoms	42,704				
Protein residues	42,704				
Ligands	0				
<i>B</i> factors (Å ²)					
Protein	90.68				
Ligand	-				
r.m.s. deviations					
Bond lengths (Å)	0.009				
Bond angles (°)	0.882				
Validation					
MolProbity score	1.96				
Clashscore	4.82				
Poor rotamers (%)	7.78				
Ramachandran plot					
Favored (%)	97.87				
Allowed (%)	7.78				
Disallowed (%)	0				

839